Controlling Material Reactivity Using Architecture

Kyle T. Sullivan, Cheng Zhu, Eric B. Duoss, Alexander E. Gash, David B. Kolesky, Joshua D. Kuntz, Jennifer A. Lewis, and Christopher M. Spadaccini*

There is an emerging interest in using advanced manufacturing methods to design and fabricate architected materials with enhanced properties.[1–5] The ability to programmably assemble materials with tailored architectures at the millimeter, micrometer, or nanometer length scales enables optimization of myriad properties including mechanical[6–9] and optical[10] properties. In this work, we investigate another area where material architecture may play a strong role: controlling the dynamic performance of materials. Reactive materials (RMs) are a class of energetic materials that, when ignited, generate an on-demand burst of energy in the form of heat and/or pressure, for example, during airbag inflation or pyrotechnic applications. RM can be divided into metal/metal (intermetallic) and metal/metal-oxide (thermite) systems, and this work focuses on the latter. Unlike high explosives, thermites do not detonate when ignited. Rather, they undergo a rapid deflagration driven by an oxidation–reduction reaction (i.e., $M_1 + M_2O \rightarrow M_2 + M_1O + \Delta E$). The linear flame propagation velocity is a commonly used metric to describe their reactivity and, to date, most research efforts have focused on enhancing kinetics by decreasing the mixing scale between constituents through mechanical milling,[11] core–shell[12] or laminate structures,[13,14] self-assembly,[15] or by replacing micrometer particles with nanoparticles.[16] While these methods have been shown to improve reactivity, further advances will likely be limited by processing constraints such as particle size, degree of mixing, passivation, sensitivity, and cost.

Here, we investigate an alternate method for controlling reactivity by creating 3D reactive material architectures (RMAs). Our work builds on recent observations that the incorporation of large, ordered pillars can have a dramatic effect on the reactivity in porous silicon-based energetics.[17] The underlying idea of RMAs is that, through precise 3D control of the placement of RM, we can exert control of the energy transport as a means to modulate the reactivity. This control would give a user an additional approach to optimize a desired output (e.g., pressure pulse, thermal pulse, etc.), without defaulting to conventional routes such as changing the RM formulation or mixing scale. Energy transport in RM involves convection of gases as well as advection of particles as gases and temperature rapidly evolve after ignition. To clarify, in this work when we use the term convection, we are referring to gas transport (convection includes both advection and diffusion by definition), and the term advection applies specifically to the transport of molten or solid particles. Formulations with excess fuel have previously been observed to outperform stoichiometric and fuel-lean mixtures due to the added gas production and enhanced convective energy transport.[18] Particle advection is also important, since small particles can be rapidly entrained by fluids and have sufficient momentum to be transported large distances.[19–22] Using RMAs, we hypothesize that both the convective and advective components of energy transport can be controlled by the architecture, so long as the architectural length scales are commensurate with the length scale over which these transport phenomena occur.

To create model RMAs, we use 3D printing to fabricate substrate architectures, followed by the deposition of RM onto the surface to a desired thickness. More details of combining these processes can be found in a previous publication.[23] Specifically, we first print a concentrated silver nanoparticle ink to produce an electrode of a predefined height, width, and shape (**Figure 1**a). The substrates are then thermally annealed at 250 °C for 30 min so that they become electrically conductive. Electrophoretic deposition (EPD) is next used to deposit an aluminum/copper oxide (80 nm Al/50 nm CuO) particulate film onto the printed electrode surfaces, either as a thin (26 μm) or thick (155 μm) film (Figure 1b). EPD has previously been shown to be a well-controlled method for depositing a precise amount of a thermite conformally onto electrode surfaces, with good mixing, yielding a highly reproducible flame propagation velocity.[24] The chosen film thicknesses are based on prior work, where thicker films were found to react nearly an order of magnitude faster than thin ones due to the increased ability to trap intermediate gases and induce local pressurization.[19,25] More importantly, at these two thicknesses the reactivity was found to be insensitive to small changes in thickness, which is important to the current work in case there are slight batch-to-batch variations in the deposited film thickness.

The two architectures examined are referred to as "channels" and "hurdles", with the primary difference being the orientation of the RM relative to the desired direction of propagation. Three parameters are investigated: i) film thickness (L_0), ii) edge-to-edge spacing between adjacent filaments (d), and iii) the orientation of the assembled material. Channel RMAs consist of two long, parallel strips, oriented in the direction of propagation, and separated by a distance d such that there is an open region in between (Figure 1c). In contrast, hurdle RMAs consist of a series of silver barriers printed in a direction 90° to

Dr. K. T. Sullivan, Dr. C. Zhu, Dr. E. B. Duoss, Dr. J. D. Kuntz, Dr. A. E. Gash, Dr. C. M. Spadaccini
Lawrence Livermore National Laboratory
Livermore, CA 94550, USA
E-mail: sullivan34@llnl.gov
D. B. Kolesky, Prof. J. A. Lewis
School of Engineering and Applied Sciences and
Wyss Institute for Biologically Inspired Engineering
Harvard University
Cambridge, MA 02138, USA

DOI: 10.1002/adma.201504286

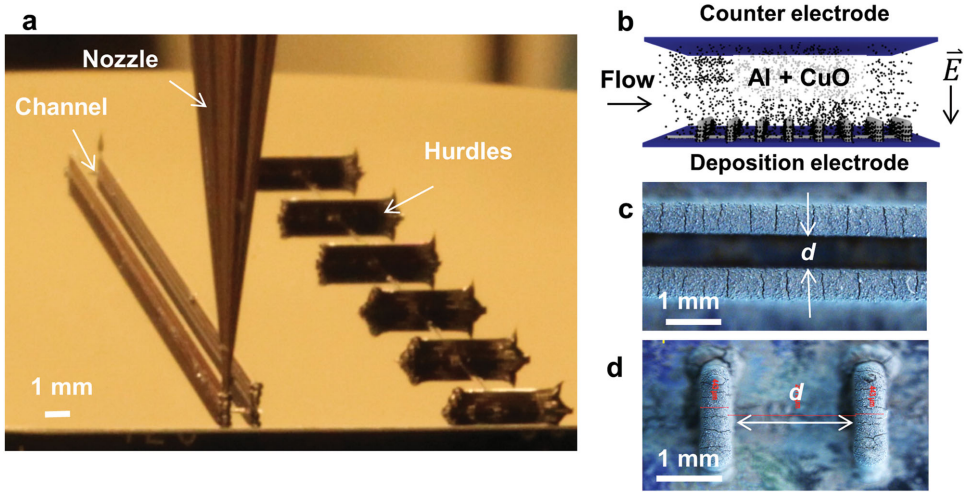

Figure 1. a) Optical image of 3D printing process for channels (left) and hurdles (right) composed of silver nanoparticle ink. The printed structures are thermally annealed to obtain conductive electrodes. b) Schematic illustration of the EPD process that is used to deposit composite Al/CuO mixtures onto the electrode surfaces. c) Optical images (top view) of a channel and d) hurdle architectures after deposition of the Al/CuO films with spacing, *d*, between the electrodes.

the direction of propagation, with a separation distance between adjacent hurdles designated as *d* (Figure 1d). To quantify the film thickness, we sectioned several thermite-coated samples for analysis. From the representative cross-sectional images shown in **Figure 2**a, we measured the film thickness and verified that the deposited coating is conformal. From the film thickness and measured deposition mass, the particle packing density is determined to be 26% of theoretical maximum density.

As a thermite reacts, a significant amount of gas is liberated, which induces a volumetric expansion process. In the case of Al/CuO, this gas could be comprised of intermediate species, such as $O_{2(g)}$, or product species such as $Cu_{(g)}$ and $Al_2O_{(g)}$. In addition to gases, there are micrometer-sized particles formed, which may include intermediate species such as $Al_{(L)}$ and $Cu_2O_{(L)}$, or product species such as $Al_2O_{3(L,s)}$ and $Cu_{(L)}$. As the film ignites and gases rapidly evolve, a multiphase expansion will occur and lift material off of the substrate. A cross-section of the initial geometry, along with the expected progression of the expansion process, is provided in Figure 2b–e. At early reaction times, the material lifts off the substrate as gases evolve, and there may be a spatial separation between the gases and particles; depending on the momentum relaxation time scale of the particles in the fluid relative to the time scale of the gas expansion (gas is shown in yellow in Figure 2c–e). At a later time, the gas-generating processes will cease and the main expansion event will stop at a final length scale, L_f. This length can be estimated using the initial film thickness L_0, volume of gas produced during the reaction, and assuming the expansion occurs normal to the surface (Figure 2f, gas production is calculated using the thermodynamic equilibrium code CHEETAH[26]). Beyond this point, particles can continue to be transported out of the gas expansion region due to their relatively large momentum (i.e., high Stokes number). The length scale over which particles can be advected ultimately depends

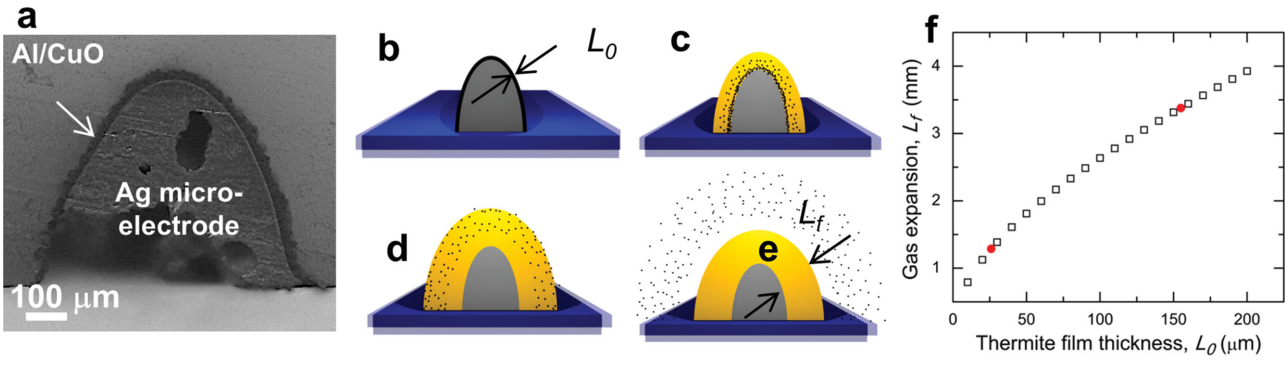

Figure 2. a) Scanning electron microscopy (SEM) image of a cross-section of a printed microelectrode that has been conformally coated with the Al/CuO composite mixture. b–e) Schematic illustrations depicting the time progression of the reaction process including unignited microelectrode coated with a thickness of thermite (b), early stage of reaction shortly after ignition showing gas expansion front (yellow) ahead of the particle front (c), intermediate stage (d) and late stage propagation where the gas production is exhausted and the particle front overtakes the gas expansion front (e). f) Plot of relationship of the gas expansion front, L_f, and thermite film thickness, L_0, calculated assuming equilibrium conditions and that the expansion occurs in a direction normal to the surface. The red markers correspond to the film thicknesses of 26 and 155 μm studied in this work.

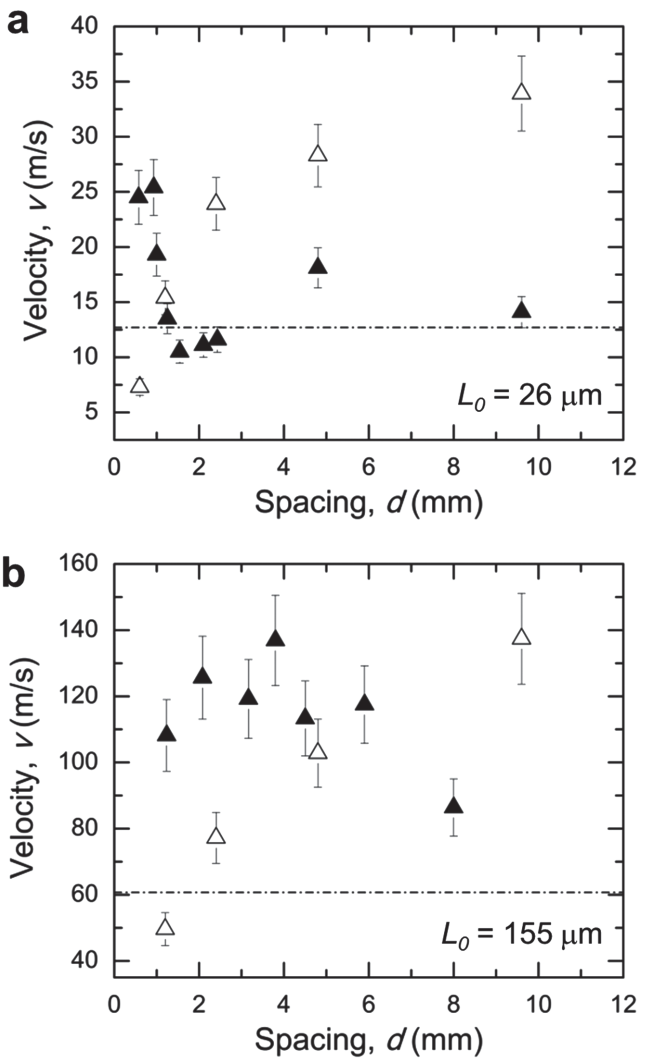

Figure 3. a,b) Flame propagation velocity as a function of *d*-spacing in channel (closed markers) and hurdle (open markers) architectures for 26 μm thick films (a) 155 μm thick films (b). The dotted lines indicate the baseline velocity of films for the given film thickness.

on their initial velocity, density, and morphology, and even a ≈100 μm film of this material has been previously observed to advect micrometer-scale particles nearly 1 cm in distance.[20]

The average flame propagation velocity, calculated from the slope of a distance time plot (see Figure S1 in the Supporting Information), is plotted as a function of edge-to-edge spacing (*d*) for the channel and hurdle architectures, as well as for thin and thick films (L_0 = 26 and 155 μm, respectively) in **Figure 3**a,b. The dotted lines in each figure correspond to baseline values, which are taken from a single strip (i.e., infinite *d*). Most striking is that the two different patterns exhibit opposite scaling behavior as *d*-spacing is changed. For channel RMAs, the propagation velocity increases above the baseline as the spacing decreases. For the thin film, this increase does not occur until the structures are brought to within ≈2 mm of one another. For the thick film, the propagation velocity increase occurs at a larger *d*-spacing of ≈8 mm. In both cases, the peak velocity is two- to threefold higher than the baseline value. For hurdle RMAs, we find the opposite effect in that the propagation velocity gradually increases as the hurdle *d*-spacing increases, again reaching values of two- to threefold higher than the baseline value. The transition spacing occurs at approximately 1 mm for thin films, and 2 mm for thick films. Note that as *d* increases, the effective velocity for hurdles is increasing even despite the fact that the mass of reactive material is decreasing. Additionally, for the hurdle RMAs, the velocity drops *below* the baseline at small *d*-spacings, indicating propagation is impeded.

Both the orientation and spacing of the RMAs can be seen to significantly impact the propagation velocity, which we claim arises due to the direction and dynamics of the multiphase expansion process. More specifically, the results are likely an artifact of how the convective and/or advective energy transport is modulated by the architecture. Still images taken from high-speed videography before and during the combustion experiments, and schematic illustrations of the proposed multiphase reaction event, are shown in **Figure 4**. For channel RMAs, the gas expansion direction is oriented perpendicular to the propagation direction, and propagates into the interstitial region. If the two channels are situated closely enough, these waves can overlap. As illustrated in Figure 4a–c, the overlap of expansion waves induces a local pressurization in the intermediate region, promoting convective transport of the hot gases in the forward direction. An animation of the proposed process is provided in Video S1 in the Supporting Information. If the channels are situated too far apart, then there will be no overlap of the gas expansion waves and two flame fronts will propagate independently (Figure 4d–f).

For hurdle RMAs, a different behavior is observed due to the expansion direction being oriented parallel to propagation. When material from a hurdle begins to react and expand, if the multiphase expansion encounters the next hurdle before it is fully developed (Figure 4g–i), then the expansion event will be physically interrupted. Also, some amount of RM on the next barrier can expand opposite to the forward direction of propagation, leading to energy pushback. Both scenarios will result in a localized pressurization in the interstitial region but, in this case, the induced pressure gradient is oriented perpendicular to the forward direction, ejecting material laterally. However, if the *d*-spacing is large enough such that the expansion can fully develop, then particles will be advected normal to the surface and in the forward direction of flame propagation (Figure 4j–l). These advected particles, which have previously been shown to achieve 2–3× higher velocities than the corresponding flame,[19] can be intercepted by the next hurdle and the process repeats. Thus, in the hurdle geometry, we observe a shift from convective to an advective mode of energy transport as the spacing increases, and concomitantly, the effective flame velocity increases. An animation of the proposed reaction process, as well as a high-speed movie, for a representative hurdle RMA in the advective transport regime is provided in Video S2 and S3 in the Supporting Information.

The observed transition points in both the channel and hurdle geometry are worth further discussion, specifically in the context of the calculated expansion length scale L_f (Figure 2f). If our hypothesis of the expansion process is correct, then L_f is a geometric parameter one can use to compare with the

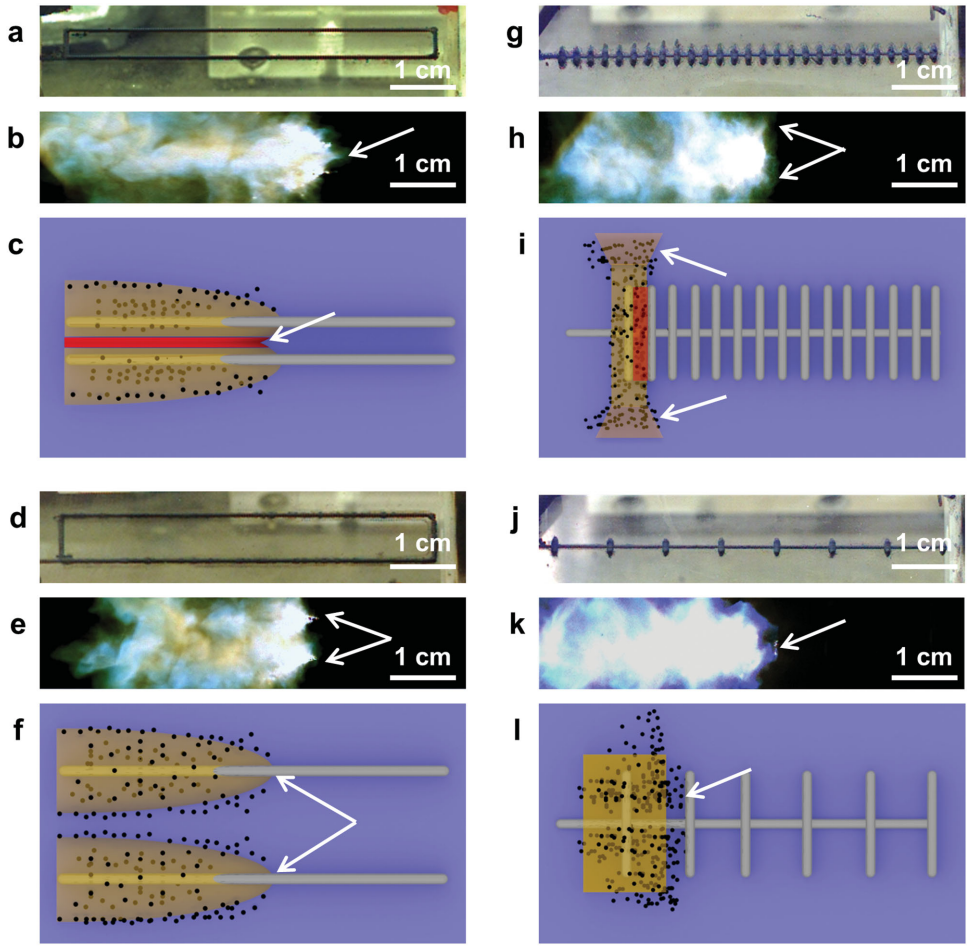

Figure 4. Combustion studies of RMAs. For schematics, particles are represented by black dots and the orange region represents the gas. a) Optical image of a channel structure with $d = 4.8$ mm, $< 2L_f$. b) Still image from high-speed videography of the combustion process for this channel structure, with arrow highlighting the formation of a jet as the expansion waves overlap and interact. c) Schematic illustration of the resultant pressurization region (red, indicated by arrow) which promotes forward convective transport. d) Optical image of a channel structure with $d = 8$ mm, $> 2L_f$. e) Still image from high-speed videography of the combustion process for this channel structure, with arrows highlighting two independently propagating fronts. f) Schematic illustration of the uncoupled reaction, with arrows highlighting the independent flame fronts. g) Optical image of a hurdle structure with $d = 2.4$ mm, $< L_f$. h) Still image from high-speed videography of the combustion process for this hurdle structure, with white arrows indicating the formation of jetting in the lateral direction. i) Schematic illustration of the interrupted expansion, inducing local pressurization in the interstitial regime and leading to lateral transport of energy, as indicated by the white arrows. j) Optical image of a hurdle structure with $d = 9.6$ mm, $> L_f$. k) Still image from high speed videography of the combustion process for this hurdle structure, with arrow showing the downstream ignition of a hurdle beyond the luminous gas expansion regime. l) Schematic illustration of the uninterrupted expansion, and the resultant advective transport and interception of particles (arrow), as facilitated by the architecture.

d-spacing. In the case of channels, we suggest that $d = 2 \times L_f$ can be used as an approximation for when interactions occurs, as this represents when the waves can physically overlap. This value agrees reasonably well with the thin film channel data. In the case of the thick film, the behavior is much more scattered and the transition point not nearly as well defined. Without confinement above the substrate, we expect the resultant pressure gradient not only to direct energy forward, but to direct it up and away from the substrate as well. Thus, the interaction is much more complex and can explain why the transition is not sharp and the data more scattered at lower values of d. In the case of hurdles, the transition d-spacings are much better defined. For this architecture, we suggest that $d = L_f$ serves as an approximation for the critical spacing, and this value again agrees well with the measured transition point for thin films, but under predicts the transition somewhat for the thick films. When the spacing between hurdles is too small ($d < L_f$), the expansion event can be physically interrupted by the next hurdle, causing pressurization in the interstitial regime and inducing lateral energy flow. However, if the spacing is large enough ($d > L_f$), the expansion can fully develop and advect particles in the forward direction towards the next hurdle, which ignites upon interception of the particles to propagate the flame.

It should be noted that the critical spacing, $d = 2L_f$ for channels and $d = L_f$ for hurdles, is important to the discussion in that it gives a user a geometric approximation for when interactions will occur. Several more experiments and considerations

would need to be done in order to improve the accuracy of this prediction. First of all, we are making an assumption that the reaction goes to thermodynamic equilibrium during the expansion, and that our calculated gas production is correct. We have assumed that the expansion only occurs normal to the surface, which is likely true near the surface but less so farther from the substrate as the volume increases and lateral flow of gases becomes possible. The printed substrates are not perfectly flat due to the nature of extrusion printing, and the substrate walls are not rectangular in the cross-section, which would simplify the geometry. Also, slight variations in film thickness may occur, particularly near edges or imperfections on the surface of the conductive substrate. With refinement in printing and deposition, along with a more detailed understanding of the dynamic pressure, temperature, and fluid properties, the multiphase flow field could be better calculated to greatly improve the accuracy of the gas expansion scale, L_f. The critical spacing could then be much better explored and our results further validated.

In this work, the chosen RMAs can yield propagation velocities below (down to ≈0.5×) or above (up to ≈3×) the nonpatterned baseline value observed for RM films. For more complex geometries involving several simultaneous expansions, it is likely that a much more dramatic effect will be seen. What limits this range for our work, especially on the upper end, is that the volume of the interaction region is small compared to the overall volume of the gas expansion. In Figure 2f, one can see that even the 26 µm thick film can expand to over a millimeter in length. Even though the feature size of the electrodes is large (Figure 2a, electrode height = 488 ± 65 µm and width = 634 ± 98 µm) relative to the initial film thickness, the interstitial volume where the interaction occurs is a small fraction of the total volume of gases produced. With more complex geometries and careful placement of RM, the influence of the architecture on energy transport could be greatly amplified as a higher fraction of energy is directed forward. Nevertheless, our observations elucidate important design parameters (orientation, d, L_0, L_f) to consider moving forward.

In summary, the effect of architecture on material reactivity is investigated using a combination of 3D printing to create conductive electrodes, followed by conformal coating Al/CuO thermite films onto the surface using electrophoretic deposition (EPD). Channel and hurdle architectures are produced, which offer different orientations of the multiphase expansion event relative to the flame propagation direction. For channel RMAs, we find that the flame propagation velocity increases as the channel spacing decreases. We propose that if two channel walls are situated closely enough ($d < 2L_f$), the expansion waves can physically overlap in the intermediate region and induce a pressure gradient to assist the forward convective transport of gases. For hurdle RMAs, if the spacing is small ($d < L_f$), the expansion is interrupted leading to lateral flow of energy and slower effective propagation velocity. If the spacing is large enough ($d > L_f$), the gas expansion is allowed to fully develop and advect particles in the forward direction, which can be intercepted downstream by the next hurdle and yield a higher propagation velocity. Our observations reveal that both the spacing and orientation of the RM features play an important role in manipulating the resultant energy transport, while offering a pathway for tailoring reactivity without using the conventional route of changing the mixing scale or formulation. We envision this control over reactivity via architected design will to lead to new types of materials for initiation systems, propellants, and pyrotechnics.

Experimental Section

See the Supporting Information for detailed experimental methods.

Supporting Information

Supporting Information is available from the Wiley Online Library or from the author.

Acknowledgements

K.T.S. and C.Z. contributed equally to this work. This work was funded by the Laboratory Directed Research and Development Strategic Initiative Program, 11-SI-004, and performed under the auspices of the U.S. Department of Energy by Lawrence Livermore National Laboratory under Contract DE-AC52–07NA27344. IM release LLNL-JRNL-678526. D.K. and J.A.L. gratefully acknowledge funding from the Department of Energy, Energy Frontier Research Center on Light-Material Interactions in Energy Conversion under Grant DE-SC0001293.

Received: September 1, 2015
Revised: October 23, 2015
Published online: December 16, 2015

[1] E. Munch, M. E. Launey, D. H. Alsem, E. Saiz, A. P. Tomsia, R. O. Ritchie, *Science* **2008**, *322*, 1516.
[2] L. J. Gibson, M. F. Ashby, *Cellular Solids: Structure and Properties*, 2nd ed., Cambridge University Press, New York **1997**.
[3] T. A. Schaedler, A. J. Jacobsen, A. Torrents, A. E. Sorensen, J. Lian, J. R. Greer, L. Valdevit, W. B. Carter, *Science* **2011**, *334*, 962.
[4] D. Jang, L. R. Meza, F. Greer, J. R. Greer, *Nat. Mater.* **2013**, *10*, 893.
[5] X. Zheng, H. Lee, T. H. Weisgraber, M. Shusteff, J. DeOtte, E. B. Duoss, J. D. Kuntz, M. M. Biener, Q. Ge, J. A. Jackson, S. O. Kucheyev, N. X. Fang, C. M. Spadaccini, *Science* **2014**, *344*, 1373.
[6] R. Lakes, *Science* **1987**, *235*, 1038.
[7] K. Bertoldi, P. M. Reis, S. Willshaw, T. Mullin, *Adv. Mater.* **2010**, *22*, 361.
[8] S. Babaee, J. Shim, J. C. Weaver, E. R. Chen, N. Patel, K. Bertoldi, *Adv. Mater.* **2013**, *25*, 5044.
[9] E. B. Duoss, T. H. Weisgraber, K. Hearon, C. Zhu, W. Small, T. R. Metz, J. J. Vericella, H. D. Barth, J. D. Kuntz, R. S. Maxwell, C. M. Spadaccini, T. S. Wilson, *Adv. Funct. Mater.* **2014**, *24*, 4905.
[10] T. Bückmann, M. Thiel, M. Kadic, R. Schittny, M. Wegener, *Nat. Commun.* **2014**, *5*, 4130.
[11] M. Schoenitz, T. S. Ward, E. L. Dreizin, *Proc. Combust. Inst.* **2005**, *30*, 2071.
[12] A. Prakash, A. V. McCormick, M. R. Zachariah, *Nano Lett.* **2005**, *5*, 1357.
[13] M. E. Reiss, C. M. Esber, D. Van Heerden, T. P. Weihs, *Mater. Sci. Eng. A* **1999**, *A261*, 217.
[14] J. S. Kim, T. LaGrange, B. W. Reed, M. L. Taheri, M. R. Armstrong, W. E. King, N. D. Browning, G. H. Campbell, *Science* **2008**, *321*, 1472.

[15] S. Apperson, R. V. Shende, S. Subramanian, D. Tappmeyer, S. Gangopadhyay, Z. Chen, K. Gangopadhyay, P. Redner, S. Nicholich, D. Kapoor, *Appl. Phys. Lett.* **2007**, *91*, 243109.
[16] C. E. Aumann, G. L. Skofronick, J. A. Martin, *J. Vac. Technol. B* **1995**, *13*, 1178.
[17] V. S. Parimi, S. A. Tadigadapa, R. A. Yetter, *J. Micromech. Microeng.* **2012**, *22*, 055011.
[18] V. E. Sanders, B. W. Asay, T. J. Foley, B. C. Tappan, A. N. Pacheco, S. F. Son, *J. Propul. Power* **2007**, *23*, 707.
[19] K. T. Sullivan, J. D. Kuntz, A. E. Gash. *J. Appl. Phys.* **2012**, *112*, 024316.
[20] K. T. Sullivan, J. D. Kuntz, A. E. Gash, *Int. J. Energ. Mater. Chem. Propul.* **2013**, *12*, 511.
[21] S. F. Son, B. W. Asay, T. J. Foley, R. A. Yetter, M. H. Wu, G. A. Risha, *J. Propul. Power* **2007**, *23*, 715.
[22] K. T. Sullivan, O. Cervantes, J. M. Densmore, J. D. Kuntz, A. E. Gash, J. D. Molitoris, *Propellants, Explos,. Pyrotech.* **2015**, *35*, 1.
[23] K. T. Sullivan, C. Zhu, D. J. Tanaka, J. D. Kuntz, E. B. Duoss, A. E. Gash, *J. Phys. Chem. B* **2012**, *117*, 1686.
[24] K. T. Sullivan, M. A. Worsley, J. D. Kuntz, A. E. Gash, *Combust. Flame.* **2012**, *159*, 2210.
[25] K. T. Sullivan, S. Bastea, J. D. Kuntz, A. E. Gash, *J. Appl. Phys.* **2013**, *114*.
[26] S. Bastea, L. E. Fried, *Chemical Equilibrium Detonation. Shock Wave Science and Technology Reference Library*, (Ed. F. Zhang), Vol. *6*, Springer-Verlag, Berlin, Germany **2012**.